frontiers in Materials

ORIGINAL RESEARCH
published: 23 November 2020
doi: 10.3389/fmats.2020.591283

Semi-Active Scissors-Seat Suspension With Magneto-Rheological Damper

Hongtao Zhu, Xiaoting Rui, Fufeng Yang, Wei Zhu and Junjie Gu*

Institute of Launch Dynamics, Nanjing University of Science and Technology, Nanjing, China

A cab seat suspension with a magneto-rheological (MR) fluid damper is introduced in this paper. A unified-format model for the MR damper is proposed to describe the dynamic characteristics of the MR damper. Also, a simple force-inverse model and a viscous damping tracking model are used for the coil current solution. A digital integrator and an extended Kalman filter are respectively adopted to obtain the vibration velocity of the chair frame and the relative motion velocity of the MR damper piston. A new skyhook control base with viscous damping tracking is applied to the semi-active seat suspension. In the simulation, compared with passive seat suspension under different displacement excitation (2, 4, 6, 8 Hz-sine, and random), the acceleration root mean square of the seat suspension with the MR damper is reduced by 52.2%, 32.2%, 41.3%, 50.8%, and 34.6%, respectively. In the experiment, the acceleration root mean square is reduced by 11.2%, 41.2%, 45.8%, and 31.5%, respectively under different displacement excitation (2, 4, 6, and 8 Hz-sine).

Keywords: magneto-rheological damper, semi-active seat suspension, skyhook control, Bingham model, Bouc-Wen model, viscous damping tracking

OPEN ACCESS

Edited by:
Xian-Xu Bai,
Hefei University of Technology,
China

Reviewed by:
Phu Xuan Do,
Vietnamese-German University,
Vietnam
Jong-Seok Oh,
Kongju National University,
South Korea

****Correspondence:***
Xiaoting Rui
ruixt@163.net

Specialty section:
This article was submitted to Smart Materials, a section of the journal Frontiers in Materials

Received: *05 August 2020*
Accepted: *14 September 2020*
Published: *23 November 2020*

Citation:
Zhu H, Rui X, Yang F, Zhu W and Gu J (2020) Semi-Active Scissors-Seat Suspension With Magneto-Rheological Damper. Front. Mater. 7:591283. doi: 10.3389/fmats.2020.591283

INTRODUCTION

Many drivers suffer from occupational diseases, including stomach disease, heart disease, and anxiety disorder. Part of those diseases are caused by the vibration of a cab. In recent years, the application of cabs has increased, so it has become necessary to reduce the vibration of cab seats by adopting some additional controllable components, of which the magneto-rheological (MR) damper is a superior candidate. An MR damper has been applied to many aspects of engineering (Choi et al., 2016), because of its advantageous features including low-power consumption, force controllability, and rapid response. The MR damper mainly consists of MR fluid which is a designable and controllable smart material whose apparent yield strength can be changed sharply within milliseconds, by the supply of an external magnet, from a free-flowing viscous liquid to a semi-solid one (Rabinow, 1951).

The nonlinear dynamic characteristics of the MR damper limit its application in engineering. In recent years, scholars have completed an extensive amount of research on the dynamic characteristics of MR dampers. Among this research, the Bingham model (Nishiyama et al., 2002; Sun et al., 2010; Fusi et al., 2014) and the Bouc-Wen model (Spencer et al., 1997; Ikhouane and Rodellar, 2005; Bahar et al., 2009; Rodríguez et al., 2009) are commonly used in applications. The Dahl model, which is used to describe solid friction (Dahl, 1976), has also been used by some scholars to describe the hysteretic characteristics of the MR damper (Spencer et al., 1997; Ikhouane and Rodellar, 2005; Bahar et al., 2009; Rodríguez et al., 2009). Neural networks models have also been applied in the modeling of an MR damper. However, the neural network lacks the necessary

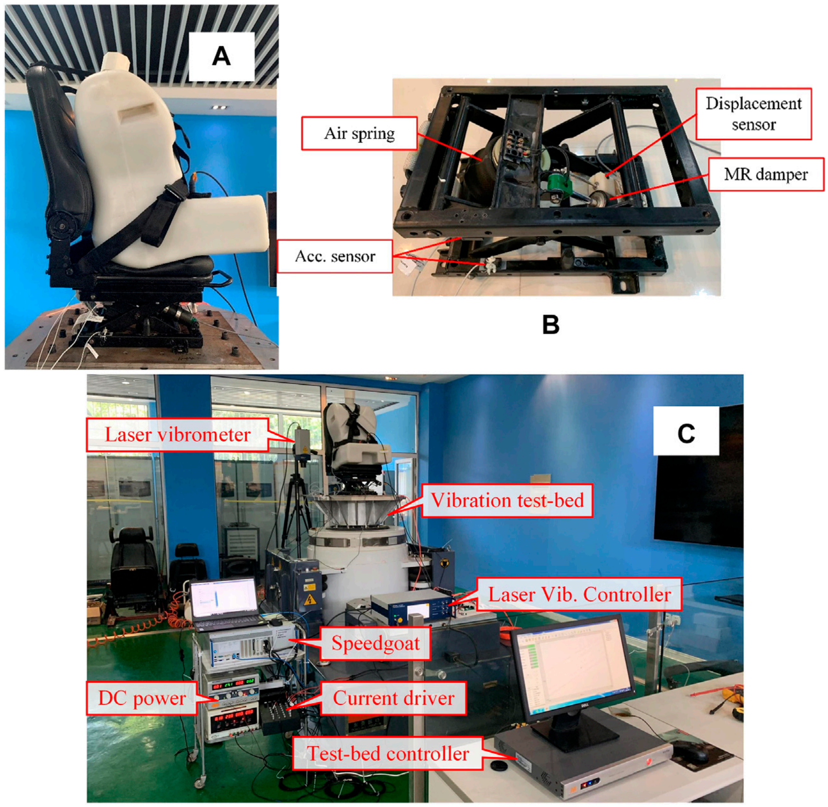

FIGURE 1 | The structure of the scissors-linkage seat suspension and experiment setup: **(A)** seat photo; **(B)** the structure of the scissors-linkage seat suspension; **(C)** the experiment setup.

physical meaning when describing the hysteresis model of the magneto-rheological damper. In most engineering applications of magneto-rheological dampers, the desired damping force needs to be converted into electric current. Therefore, an inverse model of magneto-rheological dampers is essential. Tsang et al. (2006) gives a simplified dynamic inverse model of an MR damper based on the Bingham model and the Bouc-Wen model. Also, neural network models have been widely used in dynamic inverse models (Xia, 2003; Karamodin et al., 2007; Gao and Wang, 2008; Bhowmik et al., 2010).

In semi-active seat suspension vibration isolation control, the skyhook control is still one of the main methods of the engineering application (Hatwalane, 2016). Lee and Jeon (2002) uses a 2-state skyhook control (on-off skyhook control) for seat suspension with an MR damper. Choi et al. put MR dampers into commercial seats applying the skyhook control. In Choi and Han (2007), a no-jerk skyhook control was proposed to reduce acceleration jerk. A sliding-mode control based on a human body model was used in MR damper seats in Choi and Han (2007), but it is difficult to realize in engineering. The H^{∞} control was applied to the vibration isolation control of the seat suspension with an MR damper by Yao et al. (2013). Bai et al. (2016) and Bai et al. (2017) put a rotary MR damper into the seat suspension for both longitudinal and vertical vibration attenuation. A variety of advanced controllers were designed for seat suspension with MR dampers by Phu et al. (2017), Xuan et al. (2017), and Phu et al. (2019).

In this paper, the MR damper is applied into commercial air-spring cab seats. The structure of the seat suspension used in the paper is shown in **Figure 1**. The main contributions in this paper are given as follow: 1) a unified-format model for an MR damper combining the Bingham model and the Bouc-Wen model is proposed; 2) a viscous damping tracking model based on the Bingham model is applied into a skyhook control; 3) an improved on-off control is proposed for comparison; and 4) a low-cost 3-sensor semi-active seat structure is put forward, in which the digital integrator and an extended Kalman filter are adopted for signal processing.

The paper is organized as follows: *System Configuration and Modeling* mainly introduces the system structure and system modeling; a new skyhook control is introduced in *Vibration Isolation Control*; the simulation results of sine displacement excitation and random displacement excitation are discussed in *System Simulation*; the signal processing of the sensor is given in *Signal Processing*; and the experimental results are shown in *Experiment*.

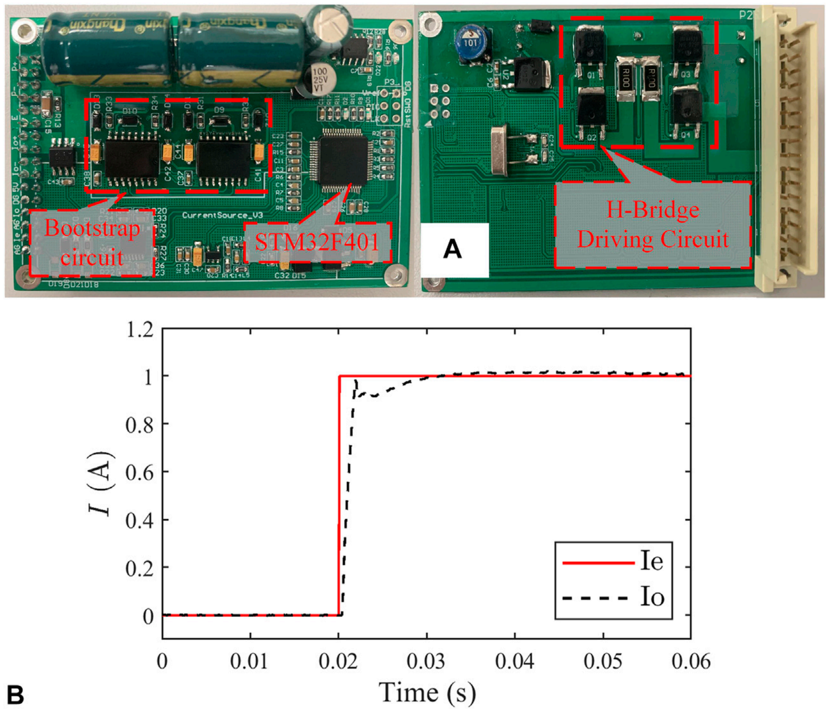

FIGURE 2 | Current driver: **(A)** PCB board; **(B)** step response.

SYSTEM CONFIGURATION AND MODELING

System Configuration

The structure of a scissors seat in this paper is given in **Figure 1B**. From **Figure 1B**, we can see that a scissors seat is mainly composed of a shear bar, an air spring, and an MR damper. The shear bar is mainly used to keep the seat mechanism stable, and the air spring is used to provide seat support rigidity. The MEMS (Micro-Electro-Mechanical System) acceleration sensor is used to measure the acceleration of the chair frame and the base, and MEMS has the advantages of long life, small size, and low price. The resistance ruler, whose accuracy can reach 0.01 mm, is used to measure the stroke of the MR damper. Also, compared to other types of displacement sensors, the resistance ruler is cheap and suitable for the market.

A coil current driver is used to provide a controlled current for the MR damper. The current driver used in this paper is composed of a power circuit, a microcontroller (MCU), a bootstrap circuit, and a H-bridge drive circuit. The microcontroller selects STM32F401 of ST Co., and its main frequency can reach up to 84 MHz. **Figure 2A** shows the PCB board of the current driver designed in this paper.

In simulation, the current driver of the MR damper is regarded as a typical 1-st system, and its transfer function is given as follows:

$$T_{cs}(s) = \frac{1}{\tau_{cs}s + 1} \tag{1}$$

where, τ_{cs} is the time constant of the coil current driver ($\tau_{cs} = 1e - 3$ s). The 1A-step response of the coil current driver is shown in **Figure 2B**.

Modeling for the Magneto-Rheological Damper System

Unified-Format Model for the Magneto-Rheological Damper

In order to facilitate the discussion, an unified-format model is established for an MR damper.

$$F_d = kz_d + c\dot{z}_d + f_c\bar{\varpi} \tag{2}$$

In **Eq. 2**, z_d is the relative displacement of damper piston, and zd is the relative velocity; k is the stiffness of the compensator in the damper (straight single-rod damper), c represents the equivalent viscous damping coefficient of the MR damper; and f_c is the coulomb friction.

When the model takes the Bingham model (Zhu et al., 2019), $\bar{\varpi} = sign(\dot{z}_d)$.

$$F_d = kz_d + c\dot{z}_d + f_c\mathrm{sign}(\dot{z}_d) \tag{3}$$

where, sign$(\cdot)$represents the sign function.

When the model takes the normalized Bouc-Wen model (Zhu et al., 2019) and there is

$$\begin{cases} F_d = kz_d + c\dot{z}_d + f_c\bar{\varpi} \\ \dot{\bar{\varpi}} = \rho\left[\dot{z}_d - \sigma|\dot{z}_d||\bar{\varpi}|^{n-1}\bar{\varpi} + (\sigma - 1)\dot{z}_d|\bar{\varpi}|^n\right] \end{cases} \tag{4}$$

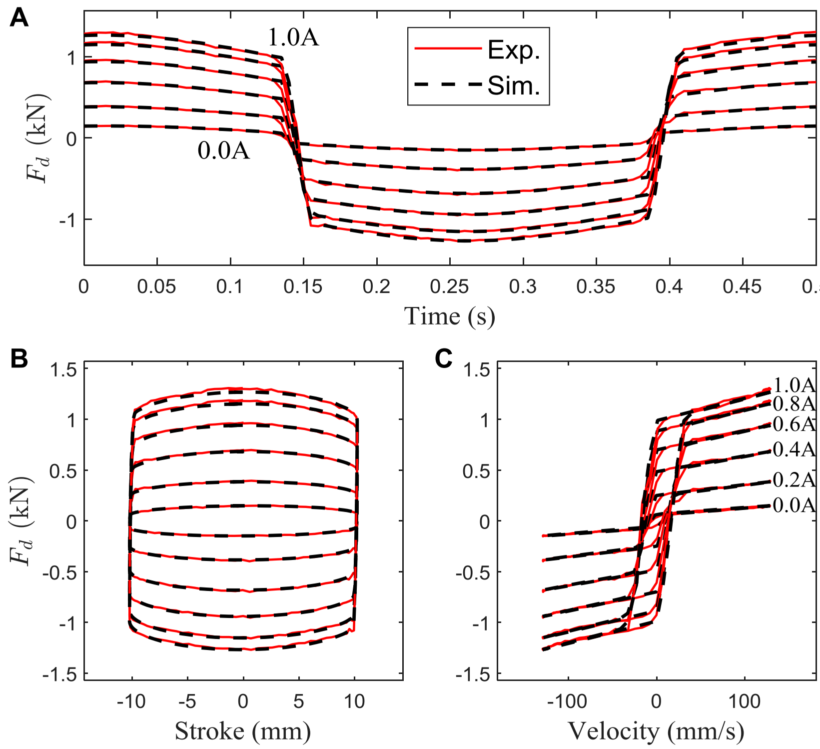

FIGURE 3 | Comparison between the predicted and experimental data (normalized Bouc-Wen model): **(A)** the damping force vs. time; **(B)** the damping force vs. stroke; **(C)** the damping force vs. velocity.

TABLE 1 | Fitting results of MR damper parameters.

Para	Value	Unit
c_1	1984.8	N · s/m
c_0	638.55	N · s/m
λ_c	1.5353	—
f_1	1336.4	N
f_0	60.331	N
λ_f	1.1943	—
ρ_1	7,018	m^{-1}
ρ_0	44,836	m^{-1}
λ_ρ	4.0485	—
k_c	1864.9	N · s/(m · A)
k_f	1041.9	N/A

In **Eq. 4**, ρ, σ, and n are the shape parameters of the normalized Bouc-Wen model. And the normalized Bouc-Wen model is stable and dissipative when $\rho > 0$, $\sigma > 0.5$, $n \geq 1$. It is not difficult to identify the parameters using the method in Zhu et al. (2019) and the comparison between the predicted and experimental data (normalized Bouc-Wen model) is given in **Figure 3**.

The exponential function is used in the parameter fitting and the fitting results are shown **Table 1**.

$$c(I) = c_1\left(1 - e^{-\lambda_c I}\right) + c_0 \tag{5}$$

$$f_c(I) = f_1\left(1 - e^{-\lambda_f I}\right) + f_0 \tag{6}$$

$$\rho(I) = \left(\rho_1 - \rho_0\right)\left(1 - e^{-\lambda_\rho I}\right) + \rho_0 \tag{7}$$

where, I represents the coil current of the MR damper.

The fit curves of parameters (ρ, σ, and n) are shown in **Figure 4** and fitting values are in good agreement with the experimental values.

When the current is small, the parameters (c and f_c) have a linear relation with the coil current of the MR damper.

$$c(I) \approx k_c I + c_0 \tag{8}$$

$$f_c(I) \approx k_f I + f_0 \tag{9}$$

Force-Inverse Model of the Magneto-Rheological Damper

The expected force of the MR damper is noted as f_e and the form of the force-inverse model is given in **Eq. 10**.

$$I_e = F_d^{-1}(f_e) \tag{10}$$

where, I_e is the expected current of the MR damper and $F_d^{-1}(\cdot)$ is the inverse model representation of the MR damper.

$$F_d(\dot{z}_d, \bar{\varpi}, I) = c(I)\dot{z}_d + f_c(I)\bar{\varpi} \tag{11}$$

At the same time, under the condition of a small current, the equivalent viscous damping coefficient c and coulomb friction force f_c still meet the linear relationship in **Eqs 8** and **9**. The expected current of the MR damper can be expressed as

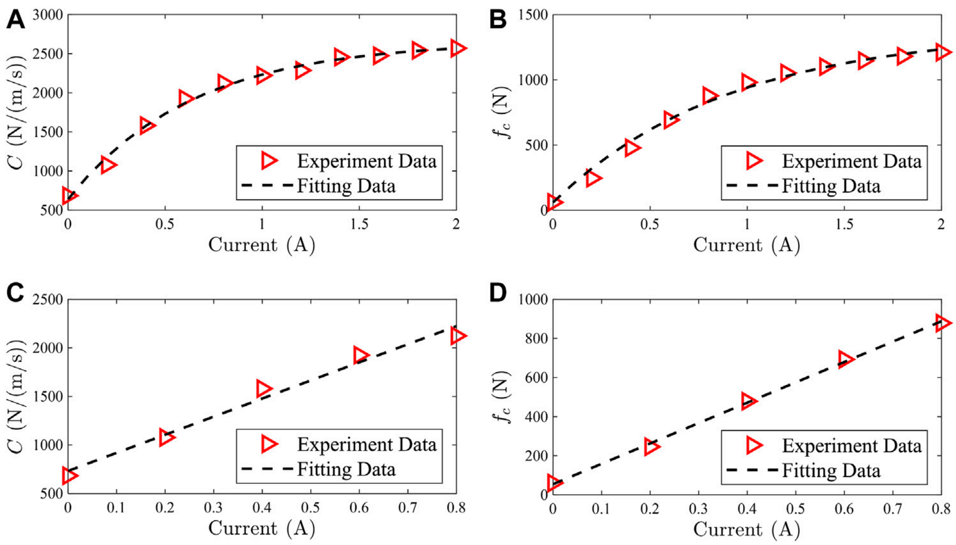

FIGURE 4 | Parameter fit curve: **(A)** nonlinear fitting of parameter c; **(B)** nonlinear fitting of parameter f_c; **(C)** linear fitting of parameter c; **(D)** linear fitting of parameter f_c.

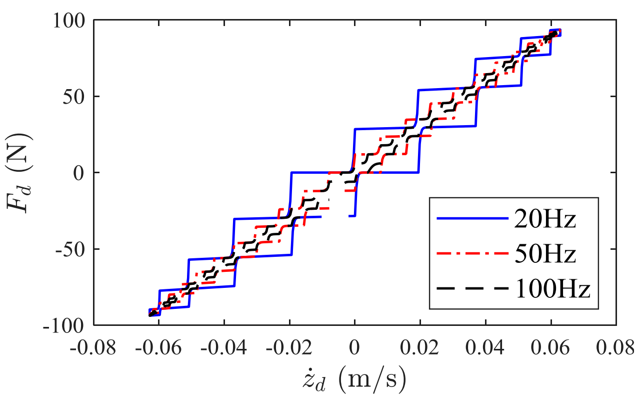

FIGURE 5 | Simulation results of viscous damper tracking.

$$I_e = \frac{f_e - c_0\dot{z}_d - f_0\bar{\varpi}}{k_c\dot{z}_d + k_f\bar{\varpi}} \tag{12}$$

When the model takes the Bingham model, $\bar{\varpi} = sign(\dot{z}_d)$, then

$$I_e = \begin{cases} 0, & |\dot{z}_d| < \varepsilon_v \ or \ (f_e - c_0\dot{z}_d - f_0\bar{\varpi})\dot{z}_d < 0 \\ \dfrac{f_e - c_0\dot{z}_d - f_0\bar{\varpi}}{k_c\dot{z}_d + k_f sign(\dot{z}_d)}, & others \end{cases} \tag{13}$$

where, $\varepsilon_v > 0$ velocity threshold constant.

Viscous Damping Tracking

Due to the energy consumption characteristics of the MR damper, it is impossible to generate the active force, so the expected force of the MR damper is the viscous damping force, which is:

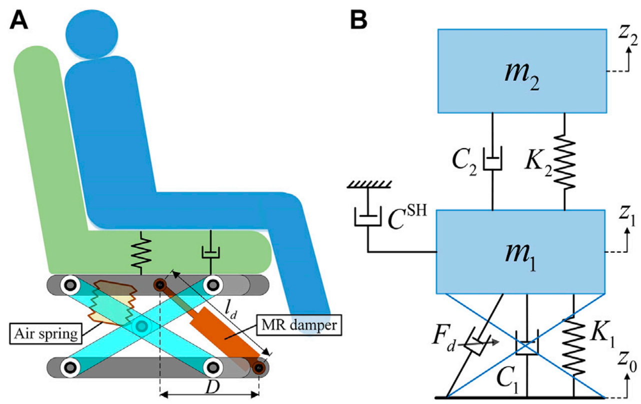

FIGURE 6 | The schematic diagram of the seat system: **(A)** the structure of the scissors-linkage seat; **(B)** the schematic diagram of the skyhook control for the seat suspension.

$$F_e = C_e\dot{z}_d \tag{14}$$

where, F_e is the expected damping force, and C_e is the expected viscous damping coefficient.

Also, according to **Eqs 8** and **9**, the expected current form of the MR damper is:

$$I_e = \frac{(C_e - c_0)\dot{z}_d - f_0\bar{\varpi}}{k_c\dot{z}_d + k_f\bar{\varpi}} \tag{15}$$

When the model takes the Bingham model, $\bar{\varpi} = sign(\dot{z}_d)$, then

$$I_e = \frac{(C_e - c_0)\dot{z}_d - f_0 sign(\dot{z}_d)}{k_c\dot{z}_d + k_f sign(\dot{z}_d)} = \frac{(C_e - c_0)|\dot{z}_d| - f_0}{k_c|\dot{z}_d| + k_f} \tag{16}$$

TABLE 2 | Parameter value of the seat suspension system.

Parameter	Value	Unit
m_1	15	kg
K_1	1.70e4	N/m
C_1	1.00e2	N/(m/s)
m_2	70	kg
K_2	3.02e5	N/m
C_2	2.14e3	N/(m/s)
C_d	4.17e3	N/(m/s)
D	0.165	m

The Bouc-Wen model is used as the accurate model of the MR damper, and the viscous damping tracking simulation is carried out under different control frequencies (20, 50, and 100 Hz). The simulation results are shown in **Figure 5**, and when the current control frequency is small, the F_d-$\dot{z}_d$ curve shows obvious serration. It is evident from **Figure 5** that the higher the control frequency, the better the viscous damping tracking effect.

Modeling for the Seat Suspension System

The schematic diagram of the seat suspension model is shown in **Figure 6**. In the schematic diagram, the seat suspension system is regarded as a 2-DOFs system.

According to the Newton formula, the dynamic equation of the seat suspension model is established as follows:

$$\begin{cases} m_2\ddot{z}_2 = -K_2(z_2 - z_1) - C_1(\dot{z}_2 - \dot{z}_1) \\ m_1\ddot{z}_1 = -K_1(z_1 - z_0) - C_1(\dot{z}_1 - \dot{z}_0) + K_2(z_2 - z_1) \\ \qquad + C_1(\dot{z}_2 - \dot{z}_1) + F_d \end{cases} \tag{17}$$

where m_1 and m_2 are the mass of the seat and the driver, respectively; z_0 is the base displacement input, and z_1 represents the displacements the seat; K_1 and K_2 represent the stiffness of airspring and cushion respectively.

$$\begin{cases} F_d = -\dfrac{\sqrt{l_d^2 - D_d^2}}{l_d}\left(c\dot{l}_d + f_c\bar{\omega}\right) \\ \dot{\bar{\omega}}(t) = \rho\left[\dot{l}_d(t) - 0.5\left|\dot{l}_d(t)\right||\bar{\omega}(t)|^{n-1}\bar{\omega}(t) + 0.5\dot{l}_d(t)|\bar{\omega}(t)|^2\right] \end{cases} \tag{18}$$

In **Eq. 18**, l_d represents the length of the MR damper and $\dot{l}_d$ is the time derivative of l_d; D is the distance constant which is defined in **Figure 6**. The expressions of l_d and $\dot{l}_d$ are given as follows:

$$l_d^2 = D_d^2 + (z_1 - z_0 + H_{10})^2 \tag{19}$$

$$\dot{l}_d = \frac{\sqrt{l_d^2 - D^2}}{l_d}(\dot{z}_1 - \dot{z}_0) \tag{20}$$

The parameter value of the seat suspension system for the simulation is given in **Table 2**.

In the above table, C_d is the viscous damping coefficient of the passive hydraulic damper, which is used for comparison with the effect of the MR damper.

VIBRATION ISOLATION CONTROL

Skyhook Control

Skyhook control (SH) is one of the most widely used control strategies in suspension control. As shown in **Figure 6B**, a hypothetical ceiling damper is placed between the seat frame and the ideal ceiling, and its damping coefficient is C^{SH}. The expected force of continuous skyhook control is noted as F^{SH}.

$$F^{SH} = -C^{SH}\dot{z}_1 \tag{21}$$

Considering the nonlinear dynamic characteristics of the MR damper, the expected current of the MR under continuous SH control is:

$$I^{SH} = F_d^{-1}\left(-F^{SH}\right) \tag{22}$$

where, $F_d^{-1}(\cdot)$ is the form of the force-inverse model which is given as **Eq. 10**

On-Off Control

When the skyhook damping coefficient C_{SH} tends to infinity, the control strategy is an on-off control strategy, and the control output switches between the maximum and the minimum. This is also called a two-state skyhook control in some literature (Choi and Han, 2007).

$$I_e = \begin{cases} I_{\min}, & \dot{z}_1\dot{z}_{10} \le 0 \\ I_{\max}, & \dot{z}_1\dot{z}_{10} > 0 \end{cases} \tag{23}$$

In order to avoid frequently switching the current output, the above formula is improved as follows:

$$I_e = \begin{cases} I_{\min}, & \dot{z}_1\dot{z}_{10} \le 0 \\ I_{\max}, & \dot{z}_1\dot{z}_{10} > 0 \text{ and } |\dot{z}_1| > \varepsilon_a \text{ and } |\dot{z}_{10}| > \varepsilon_r \\ I_{\min} + \dfrac{|\dot{z}_1|}{\varepsilon_a}I_{\max}, & \dot{z}_1\dot{z}_{10} > 0 \text{ and } |\dot{z}_1| < \varepsilon_a \text{ and } |\dot{z}_{10}| > \varepsilon_r \\ I_{\min} + \dfrac{|\dot{z}_{10}|}{\varepsilon_r}I_{\max}, & \dot{z}_1\dot{z}_{10} > 0 \text{ and } |\dot{z}_1| > \varepsilon_a \text{ and } |\dot{z}_{10}| < \varepsilon_r \\ I_{\min} + \dfrac{|\dot{z}_1\dot{z}_{10}|}{\varepsilon_a\varepsilon_r}I_{\max}, & \textit{others} \end{cases} \tag{24}$$

Where, $\varepsilon_a > 0$ is the absolute velocity threshold constant; $\varepsilon_r > 0$ is the relative velocity threshold constant is the form of force-inverse model is given in **Eq. (10)**. And, the larger the values of ε_a and ε_r, *the smoother the current output.*

Skyhook Control Based on Viscous Damping Tracking

Since $K_2 \gg K_1$, the system in **Eq. 17** can be approximated as a single-degree-of-freedom vibration system, there is:

$$m\ddot{z}_1 = -K_1(z_1 - z_0) - C_1(\dot{z}_1 - \dot{z}_0) - C_{10}(\dot{z}_1 - \dot{z}_0) \tag{25}$$

where, $m = m_1 + m_2$; C_{10} the virtual viscous damping between the seat frame and the base, which is produced by the action of the MR damper.

According to **Eq. 20**, there is:

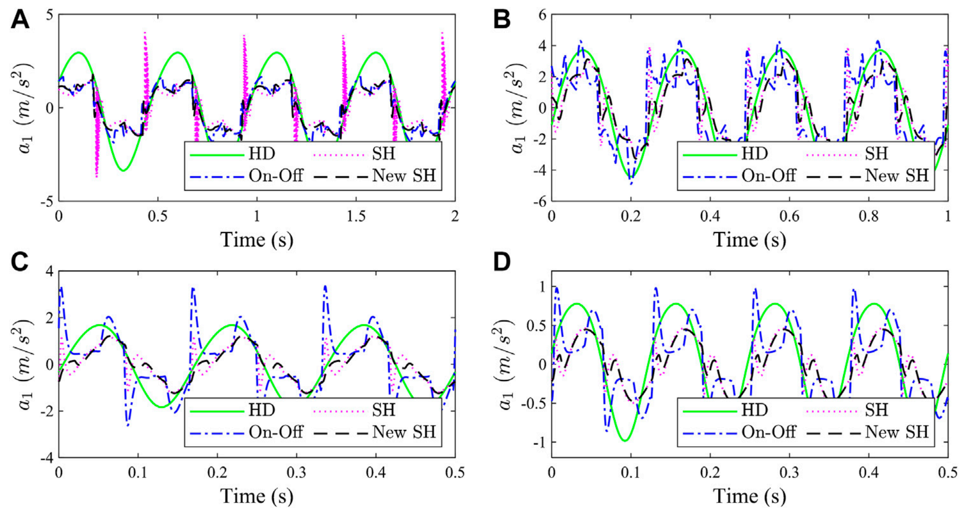

FIGURE 7 | Simulation results of sinusoidal displacement excitation: **(A)** 2 Hz, **(B)** 4 Hz, **(C)** 6 Hz, and **(D)** 8 Hz.

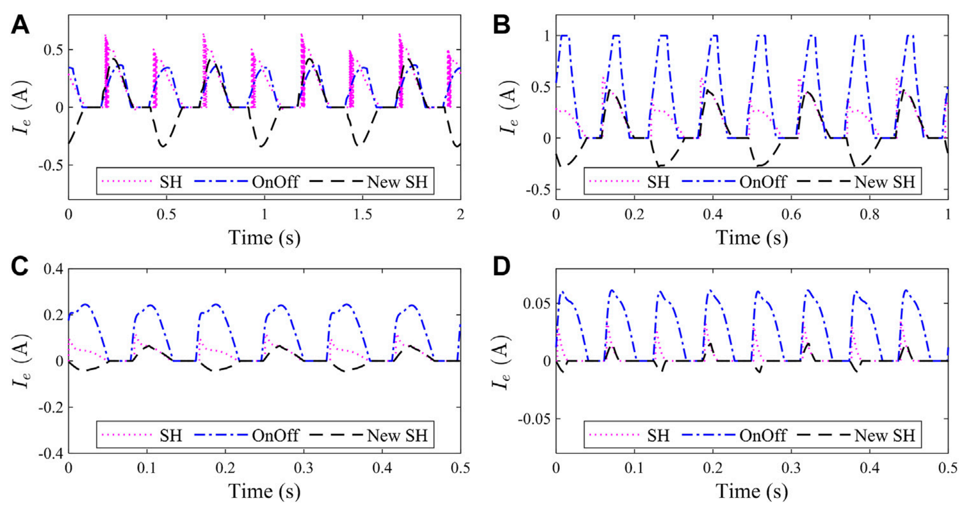

FIGURE 8 | Expected current of MR damper: **(A)** 2 Hz, **(B)** 4 Hz, **(C)** 6 Hz, and **(D)** 8 Hz.

$$C_{10} = C_{SH}\frac{\dot{z}_1}{\dot{z}_{10}} \tag{26}$$

In **Eq. 26**, $\dot{z}_{10}$ is the relative speed of the chair frame to the base, $\dot{z}_{10} = \dot{z}_1 - \dot{z}_0$.

Since the value of C_1 is small, the natural frequency and damping ratio of the single-degree-of-freedom system is given as follows:

$$\begin{cases} \omega_n = \sqrt{\dfrac{K_1}{m}} \\ \zeta = \dfrac{C_{10}}{2m\omega_n} = \dfrac{C_{10}}{c_c} \end{cases} \tag{27}$$

where, $c_c = 2m\omega_n$, is the critical damping coefficient.

The value range of C_{10} is defined as $C_{10} \in [c_{\min}, c_{\max}]$. When $C_{10} = c_c$, the system will not generate resonance, so the values range of C_{10} is given as:

$$\begin{cases} c_{\min} = 0 \\ c_{max} = c_c \end{cases} \tag{28}$$

Considering that the value of C_{10} is close to 0, there is:

$$C_{10} = \begin{cases} C_{\min}, & \dot{z}_1\dot{z}_{10} < 0 \\ C_{SH}\dfrac{\dot{z}_1}{\varepsilon_r}, & |\dot{z}_{10}| < \varepsilon_r \\ C_{SH}\dfrac{\dot{z}_1}{\dot{z}_{10}}, & others \end{cases} \tag{29}$$

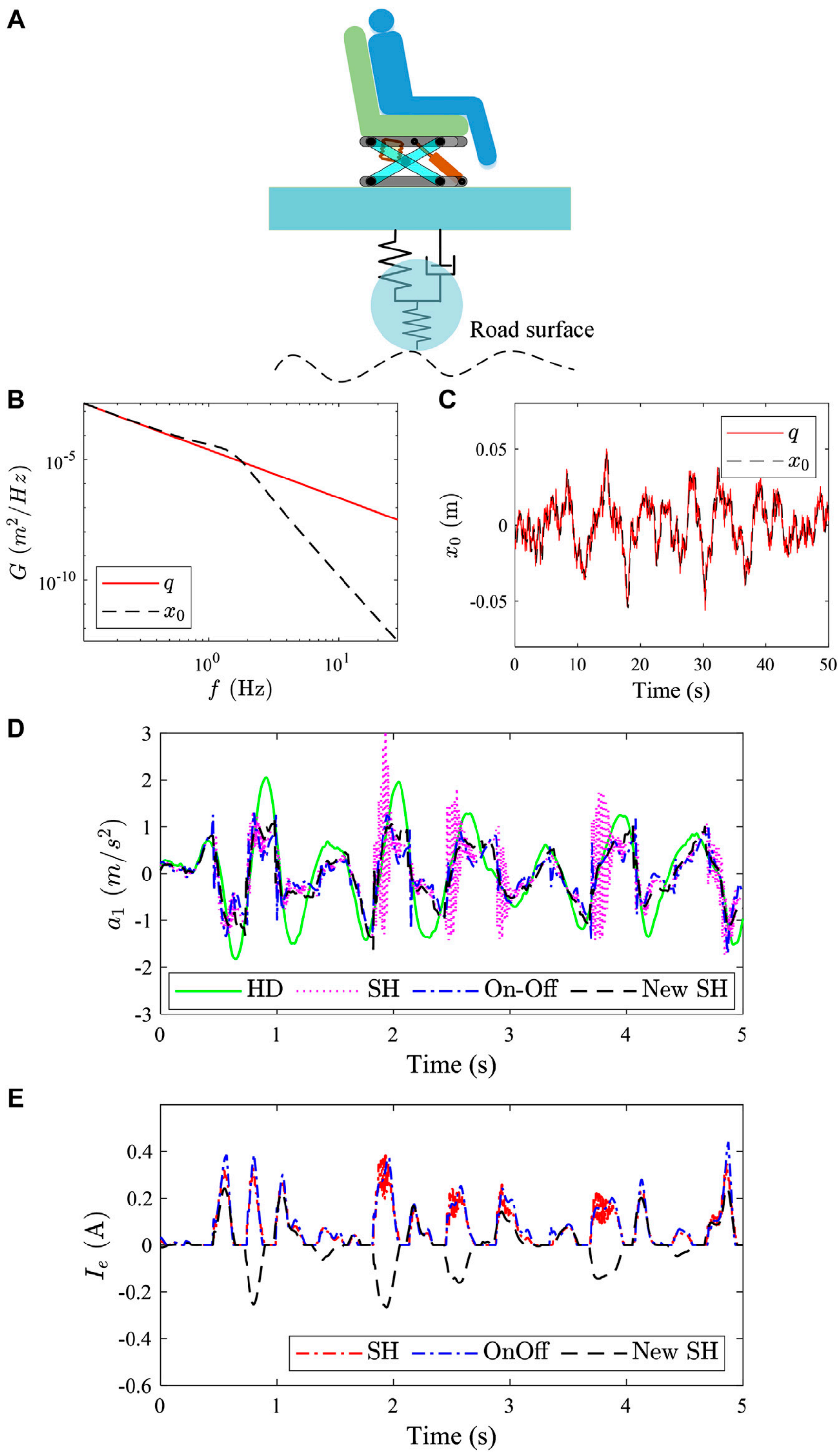

FIGURE 9 | Random input for seat suspension (*v* = 10m/s, road C): **(A)** schematic diagram of seat excitation; **(B)** displacement excitation PSD curve, **(C)** displacement excitation time-domain curve, **(D)** simulation results of seat suspension under random displacement excitation; and **(E)** expected current of the MR damper under random displacement excitation.

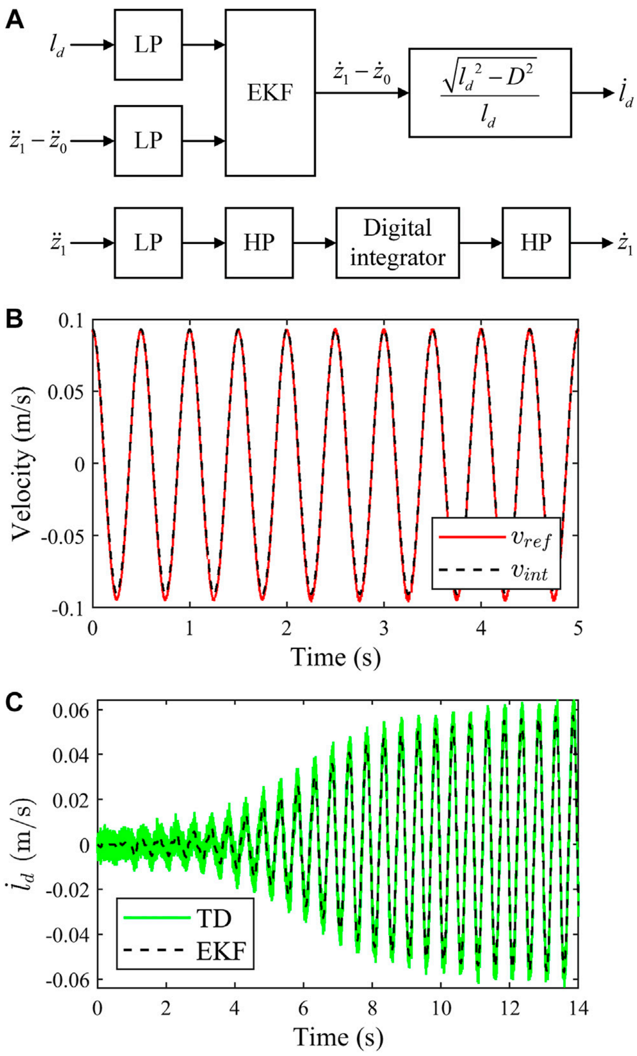

FIGURE 10 | The signal processing diagram and results: **(A)** the signal processing diagram; **(B)** acceleration signal integration results; and **(C)** EKF signal fusion results.

Bringing the value range of **Eq. 28** into **Eq. 29**, there is:

$$C_{10} = \begin{cases} c_{\min}, & C_{10} < c_{\min} \\ c_{\max}, & C_{10} > c_{\max} \\ C_{10}, & others \end{cases} \tag{30}$$

According to the seat geometry, the desired damping coefficient C_e of the MR damper is:

$$C_e = \frac{l_d^2}{l_d^2 - D^2} C_{10} \tag{31}$$

According to **Eq. 16**, the expected current of the MR damper can be obtained as follows:

$$I_e = \frac{l_d^2}{l_d^2 - D^2} \frac{C_{10}|\dot{z}_d|}{k_c|\dot{z}_d| + k_f} \tag{32}$$

If an unidirectional current is applied to the iron core of the MR damper for a long time, the iron core will have residual magnetism. In order to avoid residual magnetism of the iron core, the current direction is continuously changed during current control in **Eq. 33**.

$$I_e = I_e sign(\dot{z}_d) \tag{33}$$

SYSTEM SIMULATION

Sinusoidal Input

According to ISO2631–1, the sensitive frequency range of the human body is about 2–8 Hz. Therefore, sinusoidal base displacement (2, 4, 6, 8 Hz) is adopted to the seat displacement excitation. The simulation results of the sinusoidal displacement excitation at different frequencies is shown in **Figure 7**. In **Figure 7**, "HD" represents the passive hydraulic damper; "SH" represents the skyhook control; "On-Off" represents the on-off control; and "New-SH′ represents the skyhook control based on viscous damping tracking.

Compared with seat suspension with passive hydraulic dampers, the acceleration of the seat suspension with the MR damper, is significantly reduced under different-frequency displacement base excitation. Compared with passive suspension, under 2 Hz-sinusoidal displacement excitation, the acceleration RMS of the MR damper seat suspension with different control methods (SH, On-Off, and New-SH) decreased by 52.0%, 56.9%, and 52.2%, respectively. Under 4 Hz-sinusoidal displacement excitation, it decreased by 30.0%, 14.0%, and 32.2%. Under 6 Hz-sinusoidal displacement excitation, it decreased by 38.6%, 5.2%, and 41.3%. Under 8 Hz-sinusoidal displacement excitation, it decreased by 48.2%, 22.6%, and 50.8%. The following conclusions can be drawn from **Figure 7**: 1) the acceleration RMS reduction effect of "SH" and "New-SH" is similar, but the acceleration peak of "New-SH" is smaller; 2) the improved on-off control in this paper performs better in the low frequency (near natural frequency), but poorly in the high frequency region.

The expected current of the MR damper under sinusoidal displacement excitation is shown in **Figure 8**. Compared with the traditional skyhook control and on-off control, the expected current of the skyhook control based on viscous damper tracking is smoother. This is because the SH control proposed in this paper converts the active force into the desired damping coefficient of the MR damper, and limits the value range of the desired viscosity coefficient within a reasonable range.

Random Input

According to ISO-8608, the displacement PSD (power spectrum value) of road space surface is:

$$G_q(n) = G_q(n_0)\left(\frac{n}{n_0}\right)^{-W} \tag{34}$$

In **Eq. 34**, n represents the spatial frequency (unit: m^{-1}); n_0 represents the reference spatial frequency ($n_0 = 0.1 m^{-1}$); $G_q(n_0)$ is the displacement PSD of reference spatial frequency n_0

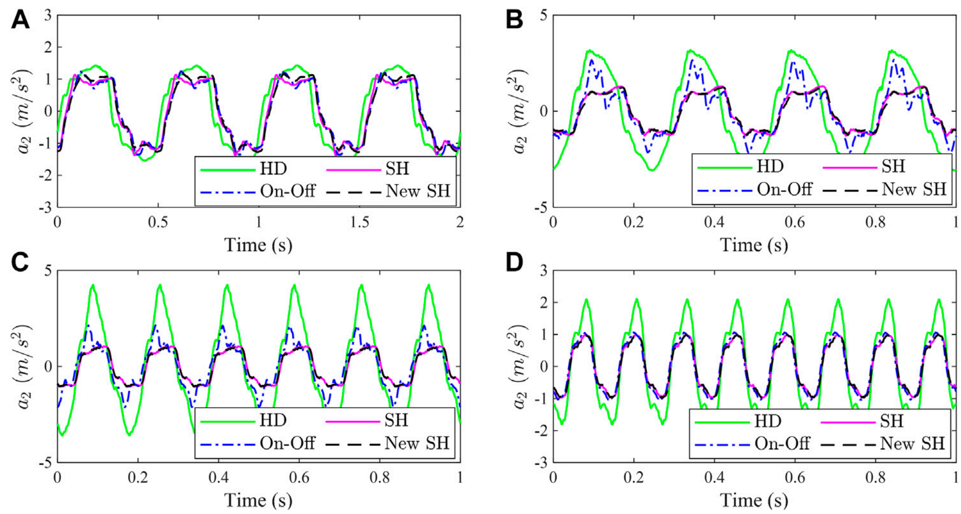

FIGURE 11 | Experimental results of sinusoidal displacement excitation: **(A)** 2 Hz, **(B)** 4 Hz, **(C)** 6 Hz, and **(D)** 8 Hz

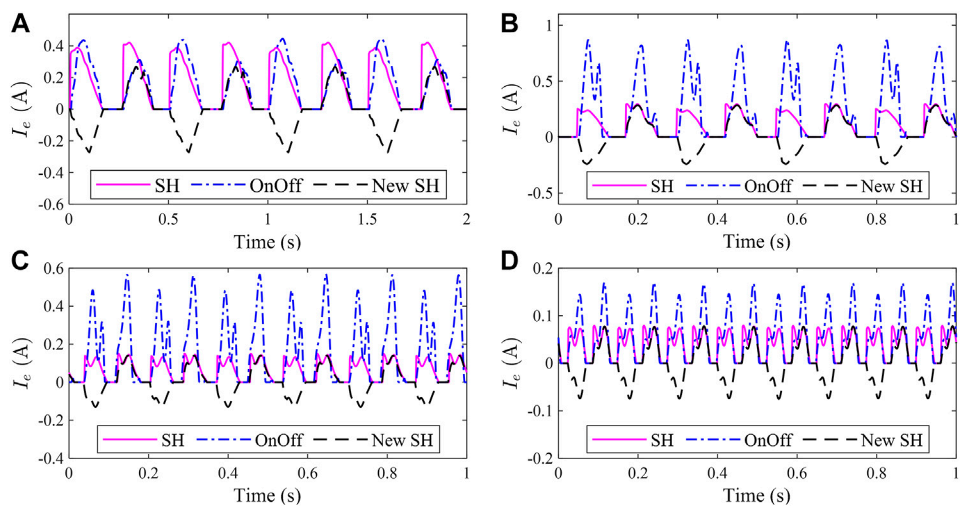

FIGURE 12 | Expected current of the MR damper: **(A)** 2 Hz, **(B)** 4 Hz, **(C)** 6 Hz, and **(D)** 8 Hz

(unevenness coefficient, unit: $\mathrm{m}^2/\mathrm{m}^{-1}$); W is the frequency index (empirical value: $W = 2$).

The vehicle speed is recorded as v and the time frequency is noted as f.

$$f = vn \tag{35}$$

Then the displacement PSD of the road time unevenness is:

$$G_q(f) = \frac{1}{v} G_q(n) \tag{36}$$

Using the sine superposition method, it is not difficult to get the time unevenness of the road surface $q(t)$:

$$q(t) = \sum_{i=1}^{N} \sqrt{G_q\left(\frac{f_i^{\mathrm{mid}}}{v}\right) \frac{\Delta f_i}{v}} \sin\left(2\pi f_i^{mid} t + \theta_i\right) \tag{37}$$

where, f_i^{mid} is the interval center frequency; Δf_i is the frequency range size; θ_i is the random phase of the sine wave, which satisfies uniform distribution on $[0, 2\pi]$.

The seat displacement excitation z_0 is actually the vibration of the body, which is the result of the action of the road surface excitation on the vehicle body through the suspension of the vehicle. Its working principle is shown in the **Figure 9**.

The filtering effect of the vehicle body on the road excitation is regarded as a typical second-order filter, and its transfer function is:

$$T_{2nd}(s) = \frac{\omega_n^2}{s^2 + 2\xi\omega_n s + \omega_n^2} \tag{38}$$

In **Eq. 38**, ω_n is the natural frequency of the typical second link, and ξ is the damping ratio. The values of ω_n and ξ can be properly

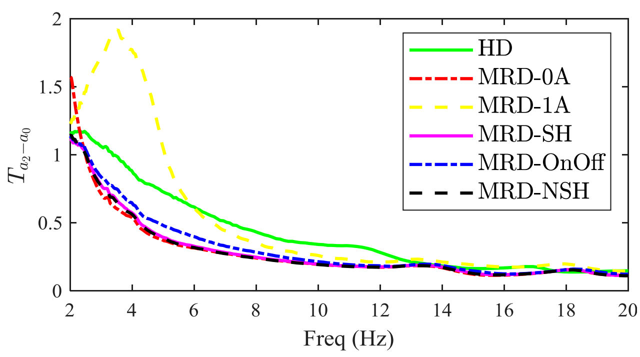

FIGURE 13 | The results of the 2–40 Hz frequency sweep experiment.

selected according to the mass of the vehicle body, and the stiffness and damping coefficient of the suspension system. $\omega_n = 9.78$ rad/s and $\xi = 0.4$ are taken in this paper.

The displacement PSD of z_0 is noted as $G_{z_0}(f)$ and there is:

$$G_{z_0}(f) = \left|T_{2nd}(j2\pi f)\right|^2 G_q(f) \tag{39}$$

when the vehicle speed is 10 m/s and the road type is C. The displacement PSD curve and time-domain curve is shown in **Figures 9B,C**.

The seat suspension simulation results under the above displacement excitation is give in **Figure 9D**. It is not difficult to conclude from **Figure 9D** that, compared with the traditional passive seat suspension, the vibration isolation effect of the seat suspension using the MR damper is significantly improved. Under the random displacement excitation in **Figure 9C**, the acceleration RMS of the seat frame is reduced by 28.0%, 38.9%, and 34.6%, respectively for those three control strategies (SH, On-Off, and New-SH).

SIGNAL PROCESSING

Figure 10A shows the block diagram of the signal processing in this paper. The seat frame acceleration signal passes through the low-pass filter (LP), high-pass filter (HP), and digital integrator in sequence to obtain the vibration velocity of the seat frame. The relative velocity of the piston of the MR damper is obtained through the extended Kalman filter (EKF).

Acceleration Signal Integration

The transfer function of the first-order high-pass filter is given as follows:

$$T_{hp}(s) = \frac{\tau_{hp}s}{\tau_{hp}s + 1} \tag{40}$$

where, τ_{hp} is the time constant of the first-order high-pass filter.

Through bilinear transformation, it is not difficult to get the discrete transfer function of the high-pass filter:

$$H_{hp}(z) = \frac{1 - z^{-1}}{\frac{T_s}{\tau_{hp}} + 1 + \left(\frac{T_s}{\tau_{hp}} - 1\right)z^{-1}} \tag{41}$$

In **Eq. 41**, T_s is the signal sampling time.

In signal integration, the following form of the digital integrator is used:

$$H_{\text{int}}(z) = \frac{T_s(z+1)}{2(z-1)} \tag{42}$$

The vibration velocity signal measured by the laser vibrometer is used as a reference signal, and the acceleration signal integration experiment results are shown in **Figure 10B**. **Figure 10B**, v_{ref} represents the velocity reference signal measured by the laser vibrometer; v_{int} is the velocity signal obtained by integrating the acceleration signal. v_{int} and v_{ref} are in good agreement in **Figure 10B**.

Extended Kalman FilterSignal Fusion

The state vector of EKF is noted as $x_k = \left[\, z_1 - z_0 + H_{10} \quad \dot{z}_1 - \dot{z}_0 \quad \ddot{z}_1 - \ddot{z}_0 \,\right]_k^T$ and the output vector is noted as $y_k = \left[\, l_d \quad \ddot{z}_1 - \ddot{z}_0 \,\right]_k^T$.

The constant acceleration (CA) model is established and T_{KF} is the sampling period of EKF. The discrete form of the CA model is given as follows:

$$\begin{cases} x_k = \Phi_{k,k-1}x_{k-1} + w_k \\ y_k = h(x_k) + v_k \end{cases} \tag{43}$$

In **Eq. 44**, w_k is the state disturbance; v_k is the measurement noise; and $\Phi_{k,k-1}$ is the state transition matrix.

$$\Phi_{k,k-1} = \begin{bmatrix} 1 & T_{KF} & T_{KF}^2/2 \\ 0 & 1 & T_{KF} \\ 0 & 0 & 1 \end{bmatrix} \tag{44}$$

$$h(x_k) = \begin{bmatrix} l_d \\ \ddot{z}_1 - \ddot{z}_0 \end{bmatrix} \tag{45}$$

$$l_d = \sqrt{(z_1 - z_0 + H_{10})^2 + D^2} \tag{46}$$

Q_k is defined as the covariance matrix of state disturbance w_k and there is:

$$Q_k = E\left(w_k w_k^T\right) = \sigma_{\ddot{a}} \begin{bmatrix} T_{KF}^5/20 & T_{KF}^4/8 & T_{KF}^3/6 \\ T_{KF}^4/8 & T_{KF}^3/6 & T_{KF}^2/2 \\ T_{KF}^3/6 & T_{KF}^2/2 & T_{KF} \end{bmatrix} \tag{47}$$

H_k is defined as the Jacobian matrix of $h(x_k)$

$$H_k = \frac{\partial h}{\partial x_k} \tag{48}$$

The steps of the EKF algorithm are given in the following equation:

$$\begin{aligned} \hat{\mathrm{x}}_{k|k-1} &= \Phi_{k,k-1}\hat{\mathrm{x}}_{k-1|k-1} \\ \mathrm{P}_{k|k-1} &= \lambda\Phi_{k,k-1}\mathrm{P}_{k-1|k-1}\Phi_{k,k-1} + \mathrm{Q}_{k-1} \\ \mathrm{K}_k &= \mathrm{P}_{k|k-1}\mathrm{H}_k\left[\mathrm{H}_k\mathrm{P}_{k|k-1}\mathrm{H}_k + \mathrm{R}_k\right]^{-1} \\ \hat{\mathrm{x}}_{k|k} &= \hat{\mathrm{x}}_{k|k-1} + \mathrm{K}_k\left[\mathrm{y}_k - \mathrm{H}_k\hat{\mathrm{x}}_{k|k-1}\right] \\ \mathrm{P}_{k|k} &= \left[\mathrm{I} - \mathrm{K}_k\mathrm{H}_k\right]\mathrm{P}_{k|k-1} \end{aligned} \tag{49}$$

In **Eq. 49**, $\hat{x}_{k|k-1}$ is the one-step state prediction; $P_{k|k-1}$ is the error variance of the one-step prediction; K_k is the Kalman filter gain;

$\hat{x}_{k|k}$ is the k-time state estimation; $P_{k|k}$ is the error variance estimation; λ is the forgetting factor which is used to improve the tracking performance of the algorithm; and R_k is the covariance matrix of measurement noise which is defined in **Eq. 50**.

$$R_k = E\left(v_k v_k^T\right) = \begin{bmatrix} r_l & 0 \\ 0 & r_a \end{bmatrix} \tag{50}$$

where, r_l is the measure error variance for the displacement sensor and r_a is the relative acceleration measurement error variance.

The experimental results of the damper piston relative velocity is given in **Figure 10C**. In **Figure 10C**, "TD" represents the result of the tracking differentiator (Wang et al., 2003) and "EKF" represents the result obtained by EKF. The experimental results show that the noise of the damper piston relative speed is smaller and the signal has a good tracking performance. **Figure 10C** shows that, adopting EKF, the relative velocity of the damper piston has smaller noise and a good tracking performance.

EXPERIMENT

Experimental Setup

As it is shown in **Figure 1C**, the experimental setup is mainly composed of DC power, a real-time control system (Speedgoat IO135 with MATLAB/Simulink, Switzerland), a laser Doppler vibrometer (LDV, type: OFV-505/OFV-5000, Polytec, Germany), a vibration test-bed, a scissors-seat with an MR damper, and a coil current driver. As a rapid control prototype, speedgoat is used to collect and store sensor signals, and output the desired current signal of the MR damper. The LDV is used to measure the vibration velocity of the chair surface as a velocity reference to verify the accuracy of the acceleration signal integration. The vibration test-bed is adopted to provide displacement excitation for the seat suspension. The current driver is used to provide controlled current for the coil of the MR damper.

Sinusoidal Input Experiment

The experimental results of sinusoidal displacement excitation are shown in **Figure 11**. Compared with passive suspension, under 2 Hz-sinusoidal displacement excitation, the acceleration RMS of the MR damper seat suspension with different control methods (SH, On-Off, and New-SH) decreased by 11.4%, 12.0%, and 11.2%, respectively. Under 4 Hz-sinusoidal displacement excitation, it decreased by 38.4%, −4.9%, and 41.2%. Under 6 Hz-sinusoidal displacement excitation, it decreased by 43.6%, 8.6%, and 45.8%. Under 8 Hz-sinusoidal displacement excitation, it decreased by 31.2%, 30.1%, and 31.5%.

The expected current of the different control strategies under sine displacement excitation are shown in **Figure 12**. Experimental results show that, compared to traditional skyhook control and on-off skyhook control, the desired current of new skyhook method based on the viscous damping tracking proposed in this paper is relatively smoother and smaller, which can reduce system power consumption to some extent.

Frequency-Sweep Experiment

The 2–40 Hz sine wave sweep excitation put into the seat suspension, and the acceleration transmission rate in frequency-domain are defined as follows:

$$T_{a_2-a_0}\left(j\omega\right) = \frac{|\mathcal{F}\left(a_2\right)|}{|\mathcal{F}\left(a_0\right)|} \tag{51}$$

where, $\mathcal{F}(\cdot)$ is the Fourier transform; a_0 and a_2 are acceleration the stiffness of base and dummy respectively; $T_{a_2-a_0}$ is the acceleration transmissibility.

Figure 13 shows the results of the 2–40 Hz frequency sweep experiment, in which "MRD-0A′ represents the MR damper with a 0 A current and "MRD-1A′ represents the MR damper with a 1A current. It can be seen from the **Figure 13** that, compared with passive suspension, the seat suspension with the MR damper has good vibration isolation performance at different frequencies.

CONCLUSION

In this work, a low-cost 3-sensor seat suspension structure with an MR damper was established, in which a digital integrator and an extended Kalman filter were adopted to enhance the signal quality in signal processing. A unified-format model for the MR damper and a viscous damping tracking model based on the Bingham model were proposed. Simulation results show that, compared to traditional skyhook control and on-off control, the new SH control with viscous damping tracking had a good performance in reducing acceleration jerk and smoothing the expected current output. However, in the experiment, the vibration isolation effect of "SH" and "New SH" was similar, and the difference between them was that the output current of "New SH" was small and smooth, which reduced the power consumption of the system to a certain extent.

DATA AVAILABILITY STATEMENT

The original contributions presented in the study are included in the article/supplementary material, further inquiries can be directed to the corresponding author/s.

AUTHOR CONTRIBUTIONS

As the first author of this paper, HZ have completed most of the work in this paper. XR, WZ, and JG funded this paper. FY assist to complete the experiment.

ACKNOWLEDGMENTS

The authors wish to acknowledge the financial support of the National Natural Science Foundation of China (Grant No. 51975298), the National Natural Science Foundation of China (Grant No. 11902158), the Natural Science Foundation of Jiangsu Province, China (Grant No. BK20181301), and the Fundamental Research Funds for the Central Universities (No. 30919011240).

REFERENCES

Bahar, A., Pozo, F., Acho, L., Rodellar, J., and Barbat, A. (2009). Parameter identification of large-scale magnetorheological dampers in a benchmark building. *Comput. Struct.* 88, 198–206. doi:10.1016/j.compstruc.2009.10.002

Bai, X. X., Jiang, P., Pan, H., and Qian, L. J. (2016). "Analysis and testing of an integrated semi-active seat suspension for both longitudinal and vertical vibration control," in *Active and passive smart structures and integrated systems 2016*. International Society for Optics and Photonics, Vol. 9799, 979921.

Bai, X.-X., Jiang, P., and Qian, L.-J. (2017). Integrated semi-active seat suspension for both longitudinal and vertical vibration isolation. *J. Intell. Mater. Syst. Struct.* 28(8), 1036-1049. doi:10.1177/1045389X16666179

Bhowmik, S., Høgsberg, J. B., and Weber, F. (2010). "Neural network modeling of forward and inverse behavior of rotary MR damper," in Proceedings of NSCM-23. The 23rd Nordic seminar on computational mechanics, Stockholm, Sweden, October 21–22, 2010. Editor A. Eriksson and G. Tibert (The Royal Institute of Technology), 169–172.

Choi, S.-B., and Han, Y.-M. (2007). Vibration control of electrorheological seat suspension with human-body model using sliding mode control, *J. Sound Vib.* 303, 391–404. doi:10.1016/j.jsv.2007.01.027.

Choi, S. B., Li, W., Yu, M., Du, H., and Do, P. X. (2016). State of the art of control schemes for smart systems featuring magneto-rheological materials. *Smart Mater. Struct.* 25, 043001. doi:10.1088/0964-1726/25/4/043001.

Dahl, P. R. (1976). Solid friction damping of mechanical vibrations. *AIAA J.* 14, 1675–1682. doi:10.2514/3.61511.

Fusi, L., Farina, A., and Rosso, F. (2014). Retrieving the Bingham model from a bi-viscous model: some explanatory remarks, *Appl. Math. Lett.* 27, 11–14. doi:10.1016/j.aml.2013.08.009.

Gao, M., and Wang, C. Z. (2008). Inverse modelling of MR damper based on ANFIS technique and its application. *J. Vib. Shock* 27(3), 140–141. doi:10.3901/CJME.2008.04.040

Hatwalane, S. (2016). "Review of driver seat suspension using MR fluid damper," in AMET-2016 (Pune, India: MIT College of Engineering). doi:10.14741/Ijcet/22774106/Spl.4.2016.66

Ikhouane, F. A., and Rodellar, J. (2005). On the hysteretic bouc-wen model. *Nonlinear Dynam.* 42, 79–95. doi:10.1007/s11071-005-0070-x.

Karamodin, A., Kazemi, H. H., Rowhanimanesh, A., Totonchi, A., and Reza, H. (2007). Semiactive control of structures using neuro-inverse mode of MR dampers. *Scientia Iranica*, 16(3). doi:10.1243/09544097JRRT240

Lee, Y., and Jeon, D. (2002). A study on the vibration attenuation of a driver seat using an MR fluid damper, *J. Intell. Mater. Syst. Struct.* 13, 437–441. doi:10.1106/104538902028606.

Nishiyama, H., Fushimi, S., and Nakano, M. (2002). Numerical simulation of MR fluid damping characteristics using a modified Bingham model. *J. Intell. Mater. Syst. Struct.* 13, 647–653. doi:10.1177/1045389x02013010007.

Phu, D. X., Quoc Hung, N., and Choi, S.-B. (2017). A novel adaptive controller featuring inversely fuzzified values with application to vibration control of magneto-rheological seat suspension system. *J. Vib. Contr.* 24(21), 5000-5018. doi:10.1177/1077546317740479.

Phu, D. X., Hung Nguyen, Q., and Choi, S.-B. (2019). New hybrid optimal controller applied to a vibration control system subjected to severe disturbances, *Mech. Syst. Signal Process.* 124, 408–423. doi:10.1016/j.ymssp.2019.01.036.

Rabinow, J. (1951). The magnetic fluid clutch. *J. Inst. Electr. Eng.* 1952, 33–34. doi:10.1049/jiee-2.1952.0007

Rodríguez, A., Iwata, N., Ikhouane, F., and Rodellar, J. (2009). Model identification of a large-scale magnetorheological fluid damper, *Smart Mater. Struct.* 18, 015010. doi:10.1088/0964-1726/18/1/015010.

Spencer, B. F., Dyke, S. J., Sain, M. K., and Carlson, J. D. (1997). Phenomenological model for magnetorheological dampers, *J. Eng. Mech.* 123, 230–238. doi:10.1061/(asce)0733-9399(1997)123:3(230).

Sun, Y., Thomas, M., and Masounave, J. (2010). A quasi-Bingham model for predicting electrorheological fluid behaviour, *Multidiscip. Model. Mater. Struct.* 6, 141–165. doi:10.1108/15736101011055301.

Tsang, H. H., Su, R. K. L., and Chandler, A. M. (2006). Simplified inverse dynamics models for MR fluid dampers. *Eng. Struct.* 28, 327–341. doi:10.1016/j.engstruct.2005.06.013.

Wang, X., Chen, Z., and Yuan, Z. (2003). Design and analysis for new discrete tracking-differentiators. *Appl. Math. Chin. Univ.* 18, 214–222. doi:10.1007/s11766-003-0027-0.

Xia, P.-Q. (2003). An inverse model of MR damper using optimal neural network and system identification. *J. Sound Vib.* 266, 1009–1023. doi:10.1016/s0022-460x(02)01408-6.

Xuan, P. D., An, J. H., and Seung-Bok, C. (2017). A novel adaptive PID controller with application to vibration control of a semi-active vehicle seat suspension. *Appl. Sci.* 7, 1055. doi:10.3390/app7101055

Yao, H. J., Fu, J., Yu, M., and Peng, Y. X. (2013). Semi-active control of seat suspension with MR damper. *J. Phys. Conf. Ser.* 412, 012054. doi:10.1088/1742-6596/412/1/012054

Zhu, H., Rui, X., Yang, F., Zhu, W., and Wei, M. (2019). An efficient parameters identification method of normalized Bouc-Wen model for MR damper. *J. Sound Vib.* 448, 146–158. doi:10.1016/j.jsv.2019.02.019

Conflict of Interest: The authors declare that the research was conducted in the absence of any commercial or financial relationships that could be construed as a potential conflict of interest.